Computers and Geotechnics 107 (2019) 97–109

Contents lists available at ScienceDirect

Computers and Geotechnics

journal homepage: www.elsevier.com/locate/compgeo

Research Paper

Implementation of a modified Drucker–Prager model in the lattice spring model for plasticity and fracture

Gao-Feng Zhao[a,*], Jijian Lian[a], Adrain Russell[b], Nasser Khalili[b]

[a] State Key Laboratory of Hydraulic Engineering Simulation and Safety, School of Civil Engineering, Tianjin University, Tianjin, China
[b] Center for Infrastructure Engineering and Safety, School of Civil and Environmental Engineering, University of New South Wales, Sydney, NSW 2052, Australia

ARTICLE INFO

Keywords:
Lattice Spring Model
Plasticity
Fracture
Drucker-Prager model
Non-associate flow rule

ABSTRACT

In this work, a general framework is developed for the incorporation of elasto-plastic constitutive models into the Distinct Lattice Spring Model (DLSM). Within this framework, a smoothed non-associative Drucker-Prager (DP) model is implemented. To verify the model, a number of numerical examples are examined, and the results are compared to the analytical solution, numerical solution based on the Finite Volume Method (FVM), and the experimental results, where available. It is shown that the proposed framework is numerically stable and is capable of solving elasto-plastic problems while maintaining the general advantages of the LSM technique in tacking material fracturing.

1. Introduction

The Lattice Spring Model (LSM) has been the subject of much interest in recent years because of its greater efficiency via modeling of fracturing without the need for remeshing [1–7]. The basic principle in LSM is to represent the global response of a solid through a group of local spring-like interactions between discrete particles. The classical LSM proposed by Hrennikoff in 1941 had a Poisson's ratio limitation that could only solve elastic problems at a fixed Poisson's ratio. Thereafter, many efforts were made to overcome this limitation, including introduction of fourth-dimensional interaction [2], angular interaction [3,5], nonlocal potential [7], and multi-body shear spring [8]. With these improved techniques, the enriched LSM could reasonably solve elastic boundary value problems over a board range of Poisson's ratios [2,7,8]. Using cohesive type constitutive models, LSMs have been successfully applied to modeling brittle and plastic fracturing of solids [5,6]. Nevertheless, the consideration of plasticity for the LSM is relatively rare because of the intrinsic incoherence between the constitutive models adopted in the LSM and the models developed for plasticity, i.e., constitutive models for the LSM are usually defined as a mathematical relationship between the displacement (a scalar) and the force (a scalar), whereas plastic models developed for continuum mechanics are functions between the strain (a 2nd order tensor) and the stress (a 2nd order tensor), which usually includes an additional variable (e.g. plastic strain) and the history dependency of the material.

The earliest work to implement plasticity into the LSM was performed by Buxton et al. [9], in which the plasticity was introduced by decreasing the elastic modulus locally while keeping the stress continuity. However, the technique could only be applied to Ramberg-Osgood-like stress-strain relation. Moreover, because of the upper bound limitation of their LSM formulation, the volume conservation under perfect plasticity was not satisfied. Chen et al. [7] overcame this difficulty by introducing a single yield parameter for the spring bond, thus limiting their model to von-Mises plasticity only. In the work of Cheng et al. [10], the Discrete Element Method (DEM) was extended to plasticity by introducing the yield criterion and the flow rule to the normal and shear springs. The von-Mises yield criterion is defined as a function of normal and shear forces, whereas the plastic flow is defined as a function of normal and shear deformation. Nevertheless, their implementation is also limited to von-Mises plasticity, and the influence of pressure cannot be considered. Other researchers have developed bond plastic models for the LSM that are used for address fracturing (e.g., [5,6,11]). However, as indicated by Buxton et al. [9], an LSM with only bond-dependent criteria would result in anisotropic plasticity, which is not acceptable, particularly for representing plasticity prior to material fracturing. The lack of a general solution for plasticity has restricted the further application of LSMs.

In this work, we develop an LSM for plasticity. First, a framework is presented for the incorporation of continuum-based plasticity models into the Distinct Lattice Spring Model (DLSM) [8]. The basic principle is to evaluate the plastic deformation of the normal and shear springs from the plastic strains of particles that are evaluated from the strain-

* Corresponding author.
E-mail address: gaofeng.zhao@tju.edu.cn (G.-F. Zhao).

https://doi.org/10.1016/j.compgeo.2018.11.021
Received 21 August 2018; Received in revised form 22 October 2018; Accepted 24 November 2018
Available online 07 December 2018

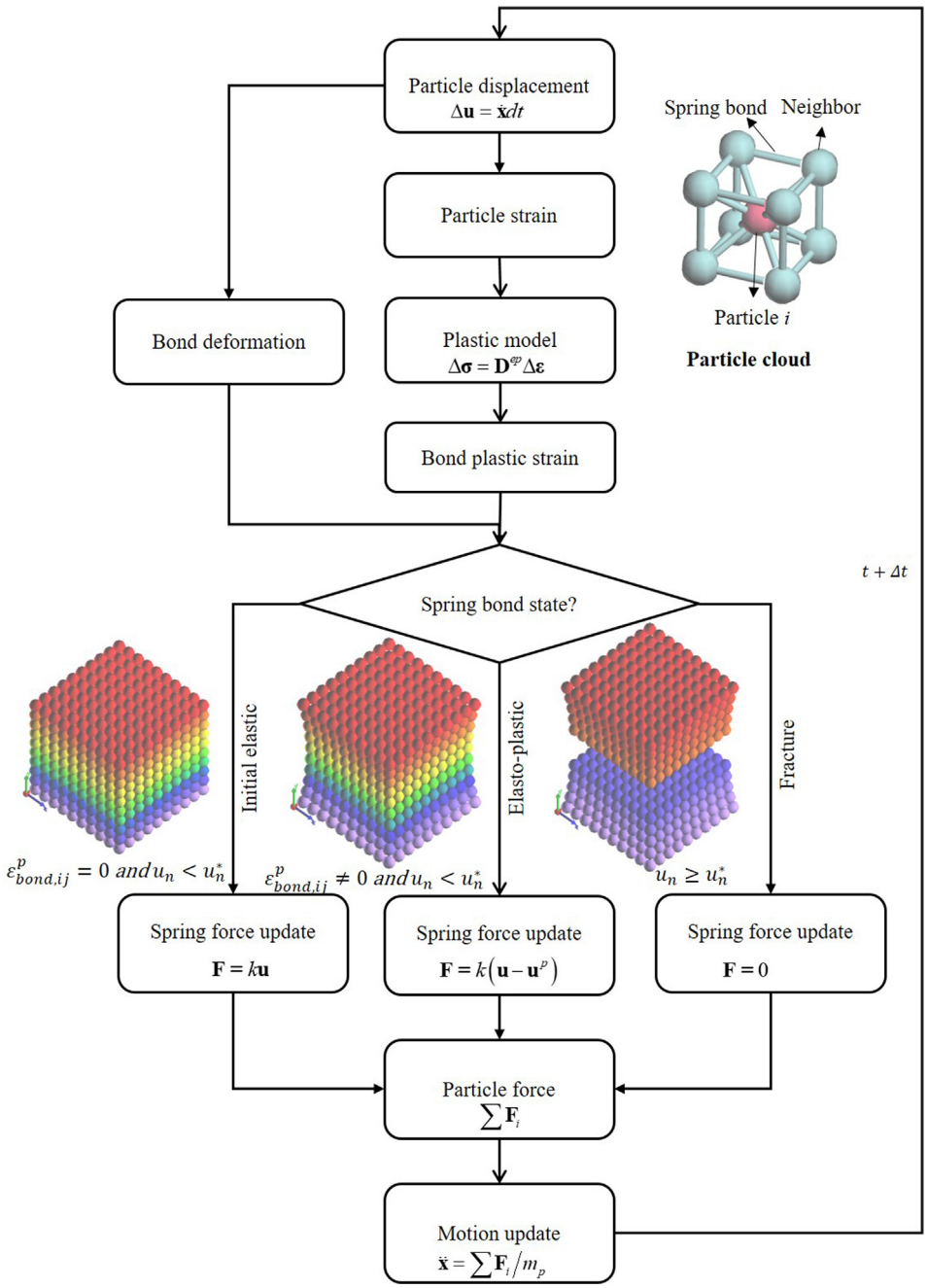

Fig. 1. Calculation cycle of the plastic DLSM.

driven plastic constitutive model. The method proposed is general, is straightforward, and can be applied to any continuum based constitutive model. As an example, a smoothed Drucker-Prager (DP) plastic model with non-associative flow rule is implemented into the DLSM. Several numerical examples are presented to demonstrate the application and the accuracy of the model.

2. The model

2.1. Plastic implementation of the distinct lattice spring model

The corresponding calculation cycle of the DLSM with the plastic constitutive model is shown in Fig. 1. Compared to the calculation cycles for the elastic DLSM [8], the main difference arises from two steps. First, given the particle displacements, which can be calculated from previous time step or prescribed boundary conditions, the plastic model is executed to obtain the particle plastic strain. Second, with the particle plastic strain and the particle displacements, the state of the spring bond is determined according to the bond's plastic strain and deformation. Then, the spring forces are calculated from the corresponding force-displacement relationship. In the DLSM, there are two springs for each bond: one is the normal spring and the other is the shear spring. To take into account the influence of plasticity, the normal and shear forces between two particles are given as

$$\mathbf{F}_{n,ij} = \begin{cases} k_n \mathbf{u}_{n,ij} & , \quad \text{initial elastic stage} \\ k_n(\mathbf{u}_{n,ij} - \mathbf{u}^p_{n,ij}) & , \quad \text{elasto - plastic stage including loading and unloading} \\ 0 & , \quad \text{fracture when } u_n > u_n^* \end{cases} \tag{1}$$

$$\mathbf{F}_{s,ij} = \begin{cases} k_s \mathbf{u}_{s,ij} & , \text{ initial elastic stage} \\ k_s(\mathbf{u}_{s,ij} - \mathbf{u}^p_{s,ij}) & , \text{ elasto - plastic stage including loading and unloading} \\ 0 & , \text{ fracture when } u_n > u_n^* \end{cases} \tag{2}$$

where $\mathbf{F}_{n,ij}$ and $\mathbf{F}_{s,ij}$ are the normal and shear forces of the bond, respectively; k_n and k_s are the normal and shear stiffnesses, respectively; $\mathbf{u}_{n,ij}$ and $\mathbf{u}_{s,ij}$ are the normal and shear deformation vectors, respectively, between particles i and j; $\mathbf{u}^p_{n,ij}$ and $\mathbf{u}^p_{s,ij}$ are the normal and shear plastic deformation vectors, respectively, between particles i and j, u_n is the deformation of the normal spring (positive in tension), and u_n^* is the ultimate deformation of the bond. In this work, we assume that the spring bond's shear deformation will cause the plastic sliding but not fracturing. The failure of the spring bond's shear spring is controlled by the total normal deformation. Herein, it should be mentioned that our framework is restricted to small deformation due to the rigid body rotation was not fully considered [2]. Moreover, we also didn't consider the coupling effect between elasticity and plasticity. The normal deformation of the spring can be further obtained as

$$\mathbf{u}_{n,ij} = ((\mathbf{u}_j - \mathbf{u}_i)\cdot\mathbf{n}_{ij})\cdot\mathbf{n}_{ij} \tag{3}$$

where $\mathbf{u}_i$and $\mathbf{u}_j$ are displacements of particle i and j, respectively; $\mathbf{n}_{ij}$ is the normal unit vector pointing from particle i to particle j that is defined as

$$\mathbf{n}_{ij} = \frac{\mathbf{x}_j - \mathbf{x}_i}{|\mathbf{x}_j - \mathbf{x}_i|} \tag{4}$$

where $\mathbf{x}_i$ and $\mathbf{x}_j$ are initial coordinates of particle i and j, respectively.

The total shear deformation of the spring is given as [8]

$$\mathbf{u}_{s,ij} = \varepsilon_{bond,ij}\mathbf{n}_{ij}l_{ij} - (\varepsilon_{bond,ij}\mathbf{n}_{ij}l_{ij})\cdot\mathbf{n}_{ij}\cdot\mathbf{n}_{ij} \tag{5}$$

where $\varepsilon_{bond,ij}$ is the total strain of the bond that can be obtained as

$$\varepsilon_{bond,ij} = \frac{\varepsilon_i + \varepsilon_j}{2} \tag{6}$$

where ε_i and ε_j are the local strain of particles i and j, respectively, which can be calculated by using a least square method. For a given particle, assume there is a particle cloud formed by itself and neighbors which have intact links with the particle (see Fig. 1). The particle cloud's deformation can be approximated by a linear function:

$$\begin{aligned} u_x &= a_1x + b_1y + c_1z + d_1 \\ u_y &= a_2x + b_2y + c_2z + d_2 \\ u_z &= a_3x + b_3y + c_3z + d_3 \end{aligned} \tag{7}$$

Its coefficients can be estimated by minimizing the quadratic equations

$$\begin{aligned} J_x &= \textstyle\sum_{j=1}^n (u_{jx} - \tilde{u}_{jx})^2 \\ J_y &= \textstyle\sum_{j=1}^n (u_{jy} - \tilde{u}_{jy})^2 \\ J_z &= \textstyle\sum_{j=1}^n (u_{jz} - \tilde{u}_{jz})^2 \end{aligned} \tag{8}$$

where u_{jx}, u_{jy} and u_{jz} are the particle's displacement components, and $\tilde{u}_{jx}$, $\tilde{u}_{jy}$ and $\tilde{u}_{jz}$ are the corresponding approximated value through the particle's displacement function as

$$\begin{aligned} \tilde{u}_{xj} &= a_1x_j + b_1y_j + c_1z_j + d_1 \\ \tilde{u}_{yj} &= a_2x_j + b_2y_j + c_2z_j + d_2 \\ \tilde{u}_{zj} &= a_3x_j + b_3y_j + c_3z_j + d_3 \end{aligned} \tag{9}$$

The coefficients are obtained as

$$\begin{aligned} (a_1 \;\; b_1 \;\; c_1 \;\; d_1)^T &= (\mathbf{A}^T\mathbf{A})(\mathbf{A}^T\boldsymbol{\beta}_1) \\ (a_2 \;\; b_2 \;\; c_2 \;\; d_2)^T &= (\mathbf{A}^T\mathbf{A})(\mathbf{A}^T\boldsymbol{\beta}_2) \\ (a_3 \;\; b_3 \;\; c_3 \;\; d_3)^T &= (\mathbf{A}^T\mathbf{A})(\mathbf{A}^T\boldsymbol{\beta}_3) \end{aligned} \tag{10}$$

where

$$\mathbf{A} = \begin{bmatrix} x_1 & y_1 & z_1 & 1 \\ x_2 & y_2 & z_2 & 1 \\ \vdots & \vdots & \vdots & \vdots \\ x_n & y_n & z_n & 1 \end{bmatrix}, \quad \boldsymbol{\beta}_1 = \begin{bmatrix} u_{1x} \\ u_{2x} \\ \vdots \\ u_{nx} \end{bmatrix}, \quad \boldsymbol{\beta}_2 = \begin{bmatrix} u_{1y} \\ u_{2y} \\ \vdots \\ u_{ny} \end{bmatrix} \quad and \quad \boldsymbol{\beta}_3 = \begin{bmatrix} u_{1z} \\ u_{2z} \\ \vdots \\ u_{nz} \end{bmatrix} \tag{11}$$

Finally, the particle's strain is calculated as

$$\begin{bmatrix} \varepsilon_{xx} \\ \varepsilon_{yy} \\ \varepsilon_{zz} \\ \varepsilon_{xy} \\ \varepsilon_{yz} \\ \varepsilon_{xz} \end{bmatrix} = \begin{bmatrix} a_1 \\ b_2 \\ c_3 \\ (a_2 + b_1)/2 \\ (b_3 + c_2)/2 \\ (c_1 + a_3)/2 \end{bmatrix} \tag{12}$$

In this work, we didn't consider the coupling effect between the elasticity and plasticity. Assume the total plastic deformation (vector) of the spring bond is

$$\mathbf{u}^p_{ij} = \varepsilon^p_{bond,ij}\mathbf{n}_{ij}l_{ij} \tag{13}$$

where l_{ij} is the initial bond, and $\varepsilon^p_{bond,ij}$ is the plastic strain of the bond, calculated as

$$\varepsilon^p_{bond,ij} = \frac{\varepsilon^p_i + \varepsilon^p_j}{2} \tag{14}$$

in which ε^p_i and ε^p_j are the plastic strain of particle i and j, respectively.

Thus, the normal plastic deformation of the bond can be obtained as

$$\mathbf{u}^p_{n,ij} = \mathbf{u}^p_{ij}\cdot\mathbf{n}_{ij}\cdot\mathbf{n}_{ij} \tag{15}$$

The plastic shear deformation is calculated

$$\mathbf{u}^p_{s,ij} = \varepsilon^p_{bond,ij}\mathbf{n}_{ij}l_{ij} - (\varepsilon^p_{bond,ij}\mathbf{n}_{ij}l_{ij})\cdot\mathbf{n}_{ij}\cdot\mathbf{n}_{ij} \tag{16}$$

Using these deformations, the contact forces between particles can be obtained, and the corresponding particle velocity and displacement can be updated via the finite central difference procedure following the steps used in the elastic DLSM [8] to perform an iteration of the calculation cycle shown in Fig. 1. To achieve the static solution, the local damping scheme is adopted as

$$\dot{\mathbf{u}}_i^{\left(t+\frac{\Delta t}{2}\right)} = \dot{\mathbf{u}}_i^{\left(t-\frac{\Delta t}{2}\right)} + \left\{\sum \mathbf{F}_i^{(t)} - \alpha\left|\sum \mathbf{F}_i^{(t)}\right| \operatorname{sgn}\left(\dot{\mathbf{u}}_i^{\left(t-\frac{\Delta t}{2}\right)}\right)\right\}\frac{\Delta t}{m_p} \tag{17}$$

where $\dot{\mathbf{u}}_i^{\left(t+\frac{\Delta t}{2}\right)}$ is the particle velocity at $t + \frac{\Delta t}{2}$, $\dot{\mathbf{u}}_i^{\left(t-\frac{\Delta t}{2}\right)}$ is the particle velocity at $t - \frac{\Delta t}{2}$, m_p is the particle mass, α is the dimensionless damping constant (set to 0.6 as default in this work), $\sum \mathbf{F}_i^{(t)}$ is the sum of forces acting on the particle, Δt is the time step, and sgn(•) denotes the function used to extract the sign. For each elemental variable, the function used to extract the sign is defined as

$$\operatorname{sgn}(x) = \begin{cases} -1, x < 0 \\ 0 \;\; , x = 0 \\ 1 \;\; , x > 0 \end{cases} \tag{18}$$

Eqs. (1)–(18) complete the procedure for implementing plasticity in the DLSM.

2.2. Smoothed Drucker-Prager model

In the following, a step-by-step application of the procedure proposed for a smoothed Drucker-Prager (DP) plastic model is presented that is applicable to a broad range of materials, e.g., metal, concrete, rock, and soil. Within this context, the yield surface is defined as

$$f(\boldsymbol{\sigma}) = \sqrt{J_2 + \delta} - A - BI_1 \tag{19}$$

where $\boldsymbol{\sigma} = (\sigma_{xx} \;\; \sigma_{yy} \;\; \sigma_{zz} \;\; \sigma_{xy} \;\; \sigma_{yz} \;\; \sigma_{zx})^T$ is the stress tensor defined at each particle, $I_1 = \sigma_{xx} + \sigma_{yy} + \sigma_{zz}$ is the first invariant of the stress

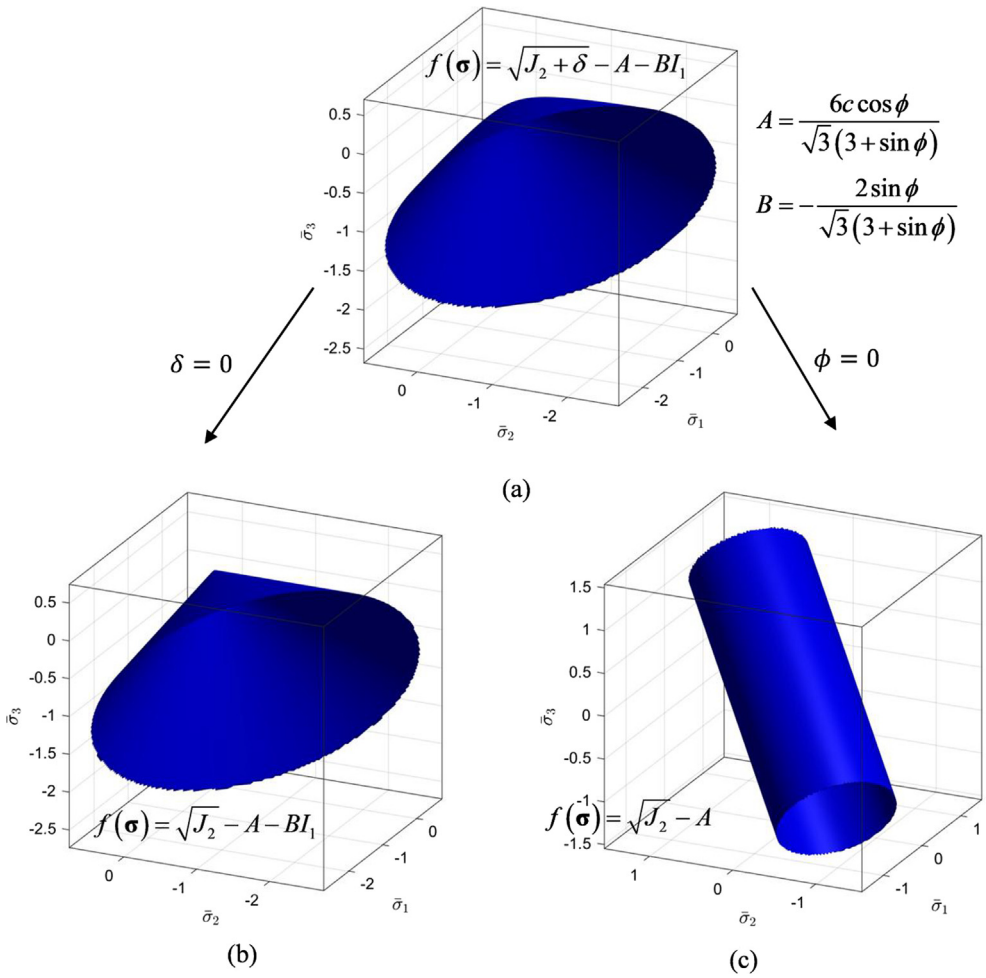

Fig. 2. The smoothed DP model in scaled principle stress space (σ_i/σ_c, where σ_c is the uniaxial compressive strength): (a) yield surface of the smoothed DP with $\delta = 0.1$, (b) the classical DP model when $\delta = 0.0$, and (c) the von-Mises model when $\phi = 0$.

tensor, and J_2 is the second invariant of the deviate stress tensor, calculated as

$$J_2 = \frac{(\sigma_{xx} + \sigma_{yy} + \sigma_{zz})^2}{3} + \sigma_{xy}^2 + \sigma_{yz}^2 + \sigma_{zx}^2 - \sigma_{xx}\sigma_{yy} - \sigma_{yy}\sigma_{zz} - \sigma_{xx}\sigma_{zz} \tag{20}$$

A and B are two coefficients of the DP model that can be related to cohesion c and friction angle ϕ through:

$$A = \frac{6c\cos\phi}{\sqrt{3}(3 + \sin\phi)} \tag{21}$$

$$B = -\frac{2\sin\phi}{\sqrt{3}(3 + \sin\phi)} \tag{22}$$

Compared with the classical DP model, the model utilized has one additional parameter δ that is introduced to avoid singularity of the normal vector at the cone tip (see Fig. 2b). A small nonnegative value is assigned to δ, which does not influence the actual prediction of the DP model. Fig. 2 shows the surface of the smoothed DP and its relationship to the classical DP and the Von-Mises models in three dimensions. At a given stress state, the corresponding normal direction at the yield surface can be obtained as:

$$\mathbf{n} = \left(\frac{\partial f(\boldsymbol{\sigma})}{\partial \sigma_{xx}} \quad \frac{\partial f(\boldsymbol{\sigma})}{\partial \sigma_{yy}} \quad \frac{\partial f(\boldsymbol{\sigma})}{\partial \sigma_{zz}} \quad \frac{\partial f(\boldsymbol{\sigma})}{\partial \sigma_{xy}} \quad \frac{\partial f(\boldsymbol{\sigma})}{\partial \sigma_{yz}} \quad \frac{\partial f(\boldsymbol{\sigma})}{\partial \sigma_{zx}}\right)^T \tag{23}$$

The plastic potential is assumed to be of the same form as the yield function, except that the friction angle is replaced with a dilation angle ψ:

$$g(\boldsymbol{\sigma}) = \sqrt{J_2 + \delta'} - A' - B'I_1 \tag{24}$$

where δ' is the smoothing parameter (e.g., 10), A' and B' are given as

$$A' = \frac{6c\cos\psi}{\sqrt{3}(3 + \sin\psi)} \tag{25}$$

$$B' = -\frac{2\sin\psi}{\sqrt{3}(3 + \sin\psi)} \tag{26}$$

The corresponding normal direction of the plastic flow at stress state $\boldsymbol{\sigma}$ is given as:

$$\mathbf{m} = \left(\frac{\partial g(\boldsymbol{\sigma})}{\partial \sigma_{xx}} \quad \frac{\partial g(\boldsymbol{\sigma})}{\partial \sigma_{yy}} \quad \frac{\partial g(\boldsymbol{\sigma})}{\partial \sigma_{zz}} \quad \frac{\partial g(\boldsymbol{\sigma})}{\partial \sigma_{xy}} \quad \frac{\partial g(\boldsymbol{\sigma})}{\partial \sigma_{yz}} \quad \frac{\partial g(\sigma)}{\partial \sigma_{zx}}\right)^T \tag{27}$$

For a given particle, the elastic stress increment within a calculation cycle can be expressed as

$$\Delta\boldsymbol{\sigma}_i^{e,t} = \mathbf{D}^e(\boldsymbol{\varepsilon}_i^t - \boldsymbol{\varepsilon}_i^{t-\Delta t}) \tag{28}$$

where $\boldsymbol{\varepsilon}_i^t$ is the particle strain at t, $\boldsymbol{\varepsilon}_i^{t-\Delta t}$ the particle strain at $t - \Delta t$, and $\mathbf{D}^e$ is the elastic matrix that is given as

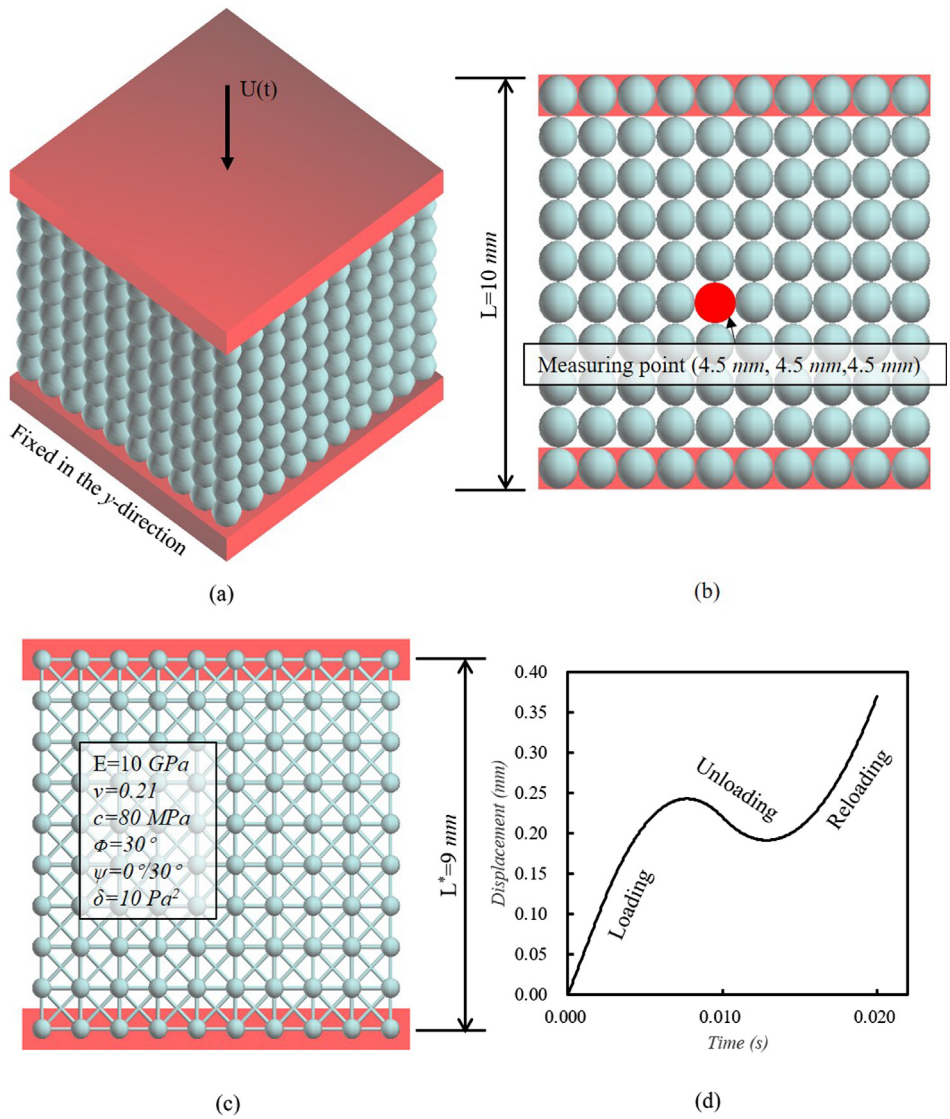

Fig. 3. Computational model of a uniaxial compression test under cyclic loading: (a) numerical model with boundary conditions, (b) the apparent length of the model and the measuring point; (c) the lattice structure and the effective length for strain calculation and (d) the displacement loading applied to the top surface.

$$\mathbf{D}^e = \begin{bmatrix} K+\frac{4}{3}G & K-\frac{2}{3}G & K-\frac{2}{3}G & 0 & 0 & 0 \\ K-\frac{2}{3}G & K+\frac{4}{3}G & K-\frac{2}{3}G & 0 & 0 & 0 \\ K-\frac{2}{3}G & K-\frac{2}{3}G & K+\frac{4}{3}G & 0 & 0 & 0 \\ 0 & 0 & 0 & G & 0 & 0 \\ 0 & 0 & 0 & 0 & G & 0 \\ 0 & 0 & 0 & 0 & 0 & G \end{bmatrix} \tag{29}$$

where K and G are the bulk and shear moduli of the particle expressed as

$$K = \frac{E}{3(1-2\nu)} \tag{30}$$

$$G = \frac{E}{2(1+2\nu)} \tag{31}$$

in which E and ν are the elastic modulus and Poisson's ratio, respectively, assigned to the particle. The normal and shear spring stiffnesses are obtained from a closed form relationship derived from strain energy equivalent principle [8]. If the particle is in the plastic state, then the stress increment within a calculation cycle is given as

$$\Delta\boldsymbol{\sigma}_i^{ep,t} = \mathbf{D}^{ep}(\boldsymbol{\varepsilon}_i^t - \boldsymbol{\varepsilon}_i^{t-\Delta t}) \tag{32}$$

where $\mathbf{D}^{ep}$ is the elasto-plastic matrix that can be obtained as

$$\mathbf{D}^{ep} = \mathbf{D}^e - \frac{\mathbf{D}^e\mathbf{m}\mathbf{n}^T\mathbf{D}^e}{\mathbf{n}^T\mathbf{D}^e\mathbf{m}} \tag{33}$$

The stress state of calculating Eq. (27) refers to the time $t-\Delta t$ that is already known in the current calculation cycle. The yield function at time $t-\Delta t$ is first calculated as

$$f_0 = f(\boldsymbol{\sigma}_i^{t-\Delta t}) \tag{34}$$

Thus, the yield function at the elastic trial stress from Equation (28) is calculated

$$f_1 = f(\boldsymbol{\sigma}_i^{t-\Delta t} + \Delta\boldsymbol{\sigma}_i^{e,t}) \tag{35}$$

As a result, the stress is updated as

$$\boldsymbol{\sigma}_i^t = \begin{cases} \boldsymbol{\sigma}_i^{t-\Delta t} + \Delta\boldsymbol{\sigma}_i^{e,t}, & f_1 < 0 \\ \boldsymbol{\sigma}_i^{t-\Delta t} + \lambda\Delta\boldsymbol{\sigma}_i^{e,t} + (1-\lambda)\Delta\boldsymbol{\sigma}_i^{ep,t}, & f_0 < 0, f_1 \geqslant 0 \\ \boldsymbol{\sigma}_i^{t-\Delta t} + \Delta\boldsymbol{\sigma}_i^{ep,t}, & else \end{cases} \tag{36}$$

where $\lambda = \frac{f_0}{f_0 - f_1}$ is a multiple to enforce return mapping when the stress state extends from the elastic to plastic region in a calculation step. With current particle stress, the corresponding particle plastic

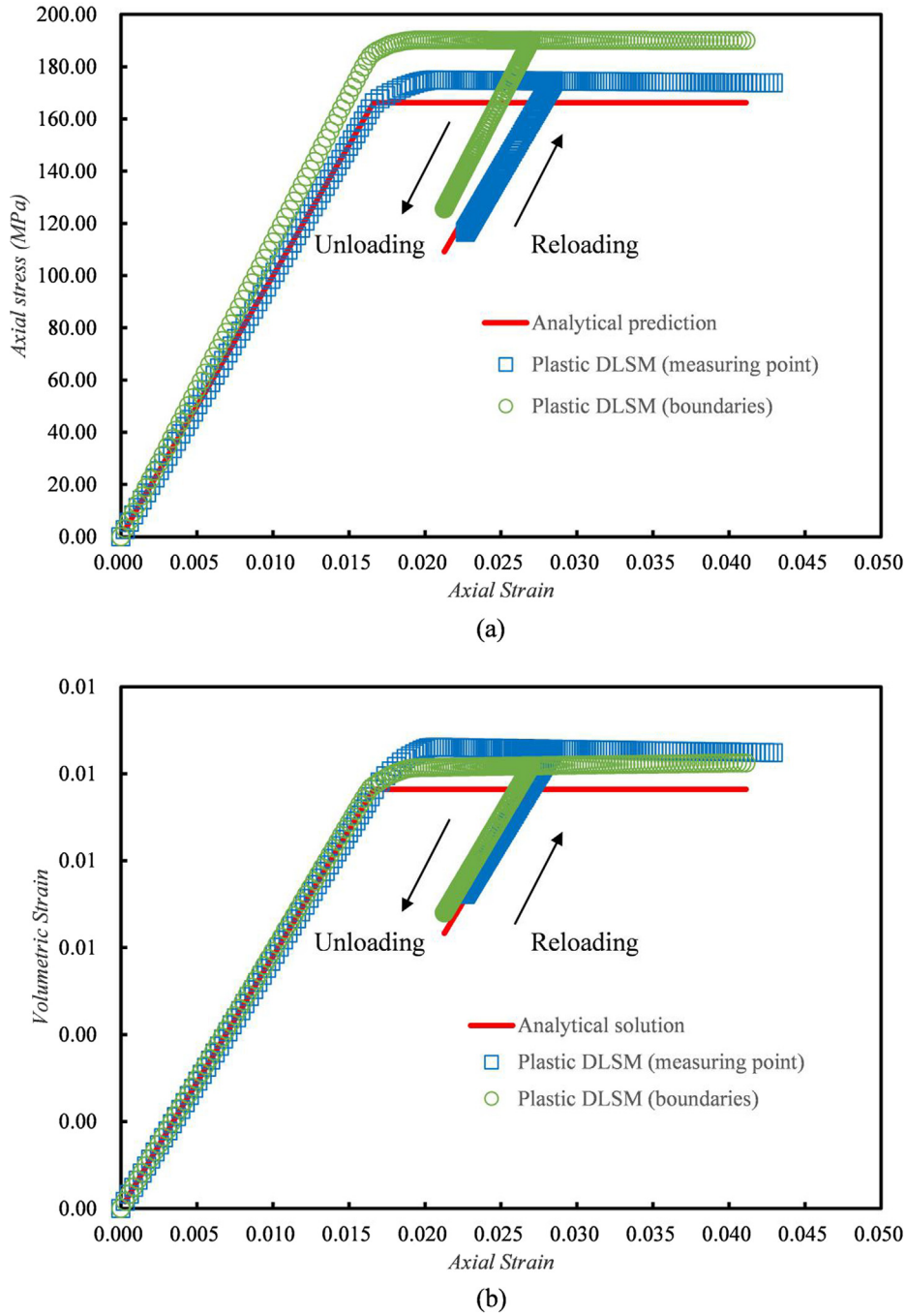

Fig. 4. Modeling results of the plastic DLSM for the uniaxial compression test with the non-associative DP model ($\phi = 30$, $\psi = 0$): (a) axial strain versus axial stress, and (b) axial strain versus volumetric strain.

strain is obtained as

$$\varepsilon_i^{p,t} = \varepsilon_i^t - [\mathbf{D}^e]^{-1}\sigma_i^t \tag{37}$$

With Eqs. (37) and (13), the corresponding plastic deformation of the spring bonds can be calculated. These steps are repeated for each of the particles, rendering the entire calculation process highly amenable to parallelization. In this work, the OpenMP is used to parallelize the code. Details of the OpenMP implementation of DLSM can be found in the work of Zhao et al. [12].

2.3. Parameters selection

In DLSM, spring parameters k_n and k_s are obtained through

$$k_n = \frac{3E}{\alpha^{3D}(1-2\nu)} \tag{38}$$

$$k_s = \frac{3(1-4\nu)E}{\alpha^{3D}(1+\nu)(1-2\nu)} \tag{39}$$

where α^{3D} is a lattice coefficient that is obtained as

$$\alpha^{3D} = \frac{\sum l_i^2}{V} \tag{40}$$

where l_i is the initial length of *i-th* spring bond, and V is the volume of the computational model. Detailed mathematic proof of Eq. (40) can be found in [8].

For the plastic DLSM, cohesive c and friction angle ϕ are the two

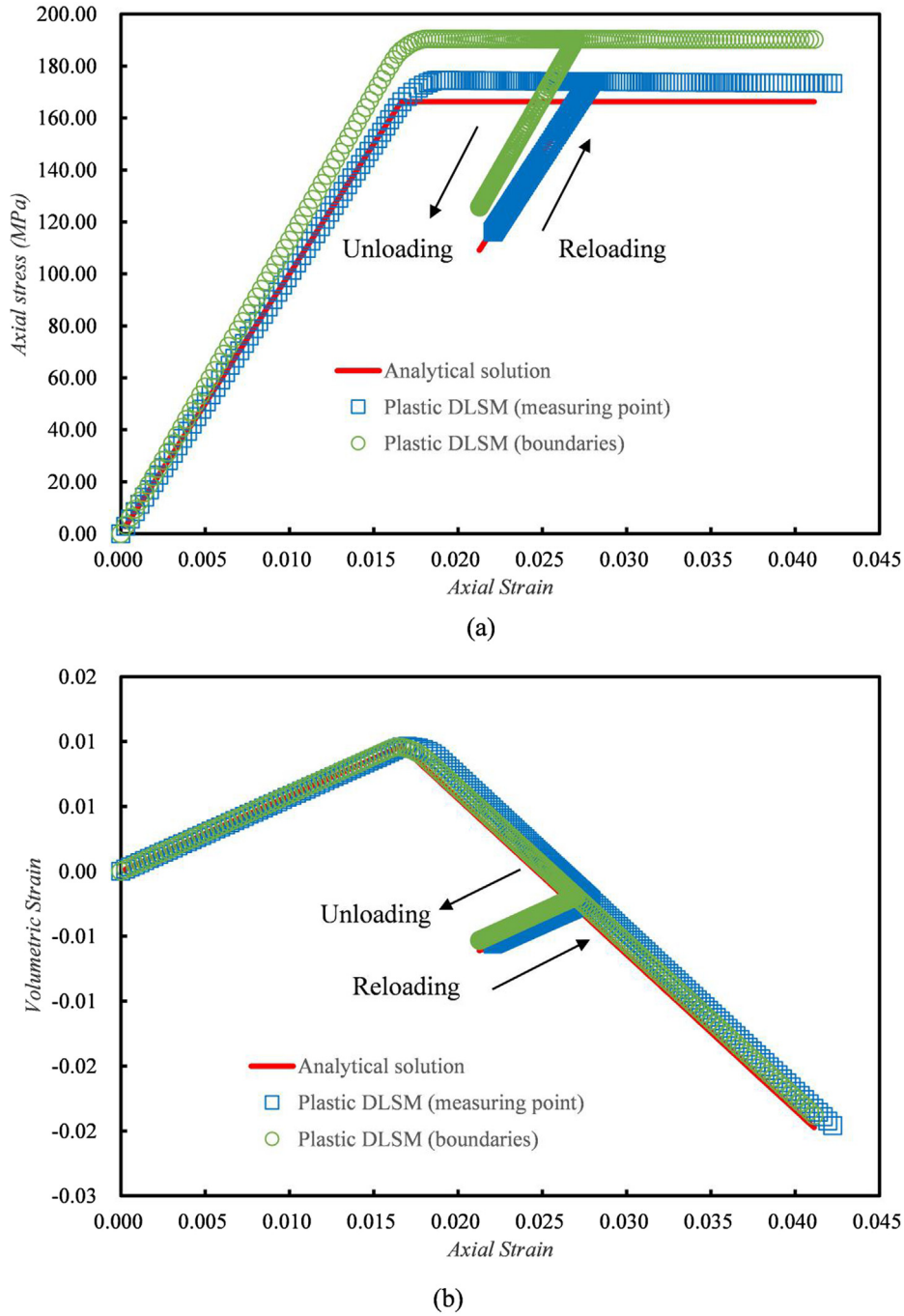

Fig. 5. Modeling results of the plastic DLSM for the uniaxial compression test with associative DP (ϕ = 30, ψ = 30): (a) axial strain versus axial stress, and (b) axial strain versus volumetric strain.

plastic parameters. The plastic bond deformation is updated according to Eqs. (13) and (37). In this sense, the plastic DLSM inherit the advantage of the original DLSM [8] in terms of directly utilizing material parameters from conventional continuum-based experiments, e.g., the elastic modulus, Poisson's ratio, cohesion and friction angle. In the elastic DLSM [8], the fracturing of solid is represented as a breakage of springs. It has been shown that the tensile normal spring failure with a deformation threshold u_n^* is an effective means to model fracturing of brittle solids [13]. In this work, we adopt the same deformation-based failure criterion for the spring bond. When the total normal deformation of a bond exceeds u_n^*, it will break and turn to contact in a manner similar to the classical DEM. In this work, we assume that the spring bond's shear deformation will cause the plastic sliding but not fracturing. The failure of the spring bond's shear spring is also controlled by the total normal deformation. To introduce heterogeneity into the computational model, a single parameter Weibull distribution function [14,15] is used to assign the randomness to the ultimate failure deformation of bonds as

$$f(\xi) = m\xi^{m-1}e^{-\xi^m} \tag{41}$$

$$u_{n,i}^* = \xi u_n^* \tag{42}$$

where ξ is a random number that satisfies the distribution function of Eq. (41) and m is the shape factor that describes the heterogeneity of breakage deformation of spring bonds. Note that this heterogeneity only influences the failure and not the deformation. Therefore, the

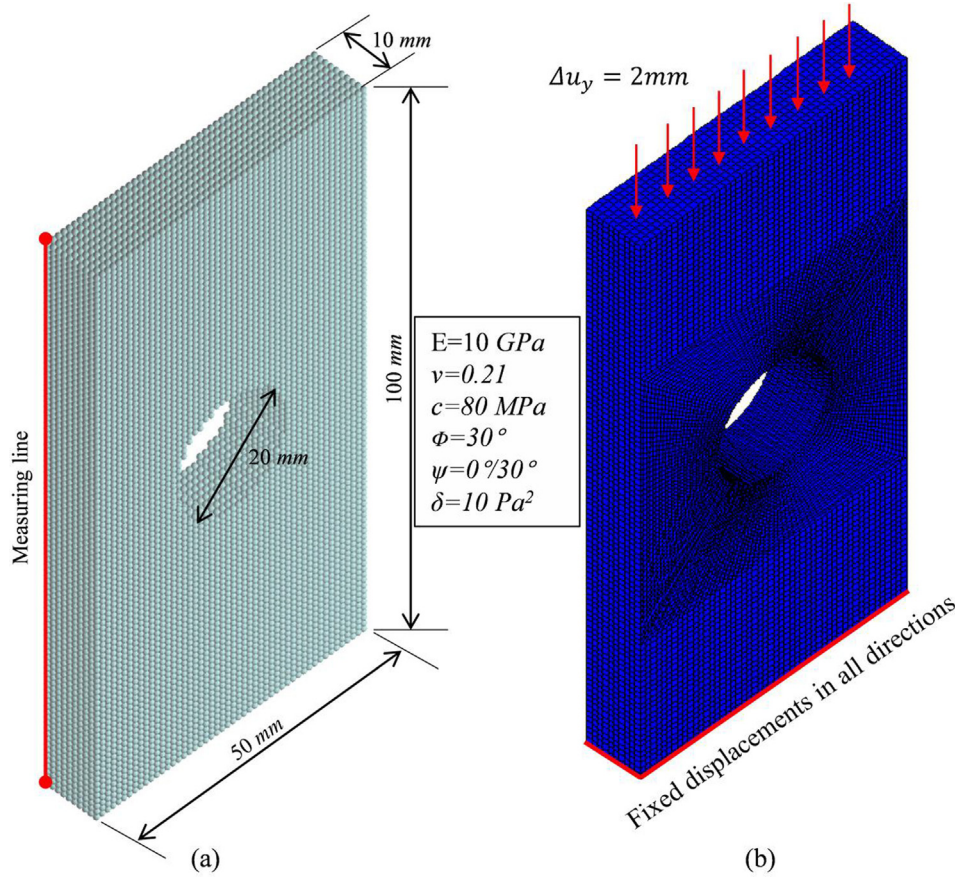

Fig. 6. The DLSM and FVM computational models for a plastic boundary value problem: (a) model dimensions (the same as those applied for the FVM counterpart), and (b) boundary conditions (the same as those applied to the DLSM counterpart).

model remains homogenous prior to fracturing, which might be not applicable for rock-like materials. In summary, there are two parameters for the elastic response, two parameters for the plastic response, and two parameters for fracturing. With these six parameters, the plastic DLSM will be able to describe problems in elasticity, plasticity and fracturing. A calibration process is required for the two fracture related parameters, which will be illustrated in Section 3.4.

3. Numerical examples

To examine numerical stability and accuracy of the model proposed, solutions to a number of boundary values problems are obtained and compared to known analytical or numerical solutions. Experimental data are also presented where available. The following examples are considered: (1) Uniaxial Compressive Strength (UCS) testing of a cube under cyclic loading, (2) compression of a plate with circular hole, (3) cylinder tunnel excavation in an infinite medium, and (4) fracturing of a titanium alloy plane subject to tensile loading.

3.1. UCS testing of a cube under cyclic loading

In this example, as shown in Fig. 3, a UCS testing of a cube under cyclic loading is conducted. The bottom surface of the cube is fixed in y-direction, and a cyclic loading (see Fig. 3d) is applied to the top surface. The problem considered consists of a cube with dimensions: 10 mm × 10 mm × 10 mm using a particle size of 1 mm. The material parameters are $E = 10$ GPa, $\nu = 0.21$, c = 80 MPa, $\phi = 30°$, and$\psi = 30°/0°$. There is a total number of 1000 particles. The Cubic II lattice is selected in this example because it has already been proven as a simple lattice configuration that can model the isotropic linear elasticity [8] and the crack propagation of brittle solids [13] among other cases. In this work, we adopt this lattice configuration for all the simulations. However, the selection of different lattice configurations is also feasible for DLSM.

Note that boundary conditions can only be applied to the center of the particles. Therefore, the effective length (see Fig. 3c) for strain calculation is adopted as L-D = 9 mm, where L is the size of the specimen, and D is the diameter of the particle. A measuring point (see Fig. 3b) is inserted into the computational model to obtain the history of strain and stress of the measuring particle. In addition, the strain and stress of the numerical simulation can be obtained from the displacement and loading force history recorded in the boundaries; this approach is similar to the physical uniaxial compression test. The strains are calculated as

$$\varepsilon_x = \frac{u_x^R(t) - u_x^L(t)}{L^*} \tag{43}$$

$$\varepsilon_y = \frac{u_y^T(t) - u_y^B(t)}{L^*} \tag{44}$$

$$\varepsilon_z = \frac{u_z^F(t) - u_z^B(t)}{L^*} \tag{45}$$

where $u_x^R(t)$ and $u_x^L(t)$ are the average displacement in the x-direction of the right and left surfaces of the cube, respectively; $u_y^T(t)$ and $u_y^B(t)$ are the average displacement in the y-direction of the top and bottom surfaces of the cube, respectively; $u_z^F(t)$ and $u_z^B(t)$ are the average displacement in the z-direction of the front and back surfaces of the cube, respectively; and L^* is the effective length of the cube. The stress is obtained as

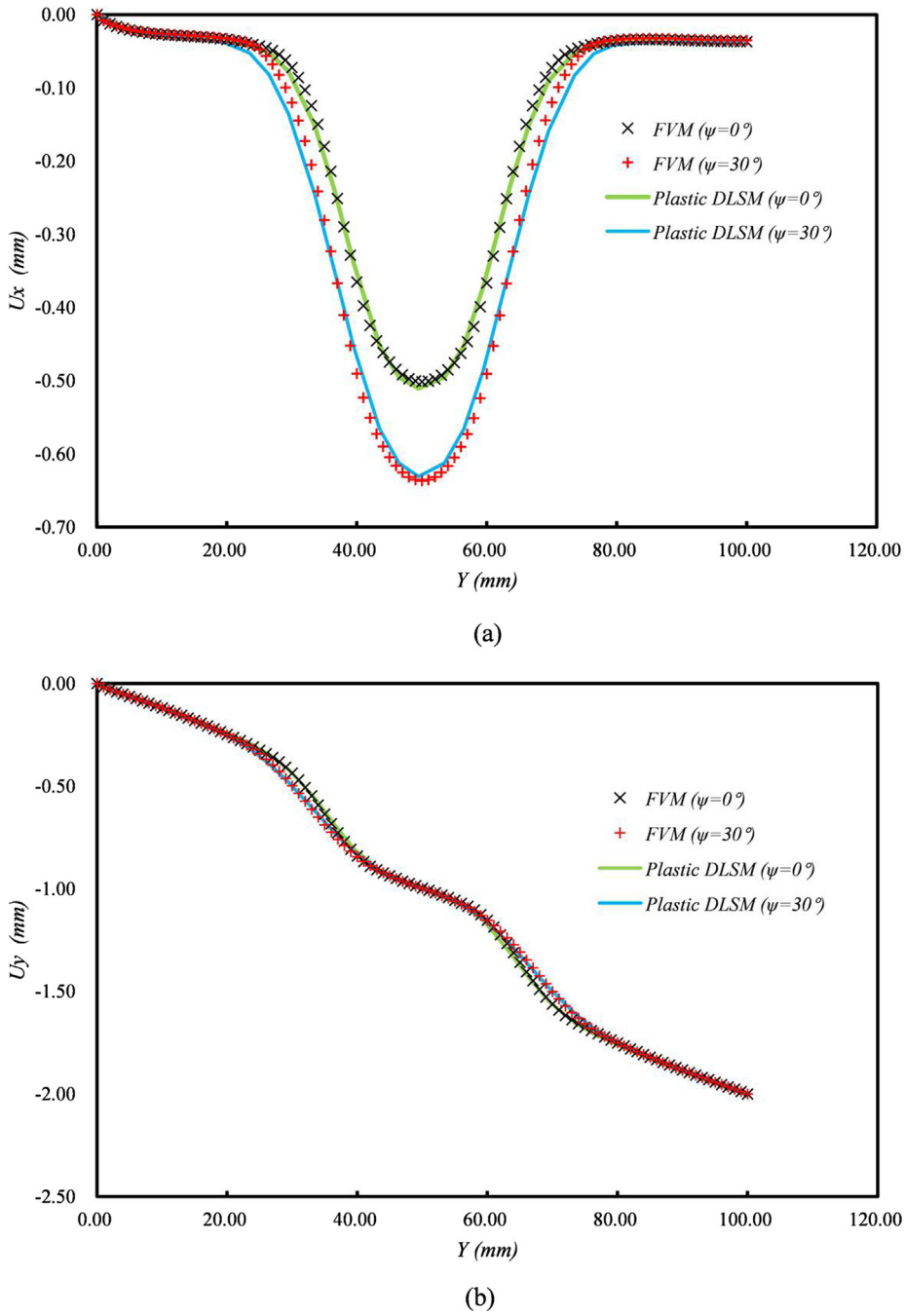

Fig. 7. Comparison between the displacements predicted by the plastic DLSM and FVM: (a) displacement in the *x*-direction along the measuring line, and (b) displacement in the *y*-direction along the measuring line.

$$\sigma_y = \frac{F_y^T(t)}{L^2} \tag{46}$$

where $F_y^T(t)$ is the reaction force in the *y*-direction of the cube's top surface, and L is the length of the cube. Two different strain-stress curves will be obtained from the numerical simulation (one from the measuring point and the other from the boundaries). As a comparison, a program using the DP constitutive model for a single stress point under the cyclic uniaxial compression test is implemented into *Matlab*. The corresponding strain-stress curves under the cyclic strain loading is calculated and used as the reference data for verification.

Fig. 4 shows the results of the DLSM with the non-associative DP model ($\phi = 30^\circ$ and$\psi = 0^\circ$). The first conclusion is that the algorithm is numerically stable, and the loading-unloading-reloading behavior can be well captured. From Fig. 4b, the volume conservation is also well reproduced. Fig. 5 further lists the numerical results and the corresponding analytical results of the associative DP model; these results also show general good fitting over the analytical prediction. We can conclude that the smoothed DP model is well implemented to the DLSM. A difference is found between the analytical prediction and the numerical prediction because the deformation within the cube is not perfectly homogenous. The uniaxial compression test is a 3D boundary value problem for DLSM simulation. As shown in Fig. 3c, these particles at the surface have different connections compared with these in the middle of the cube. Therefore, the model is not completely mechanically homogenous, and a deviation is expected for the numerical simulation compared with the analytical solution from the constitutive model. The mismatch between strain-stress curves obtained from the

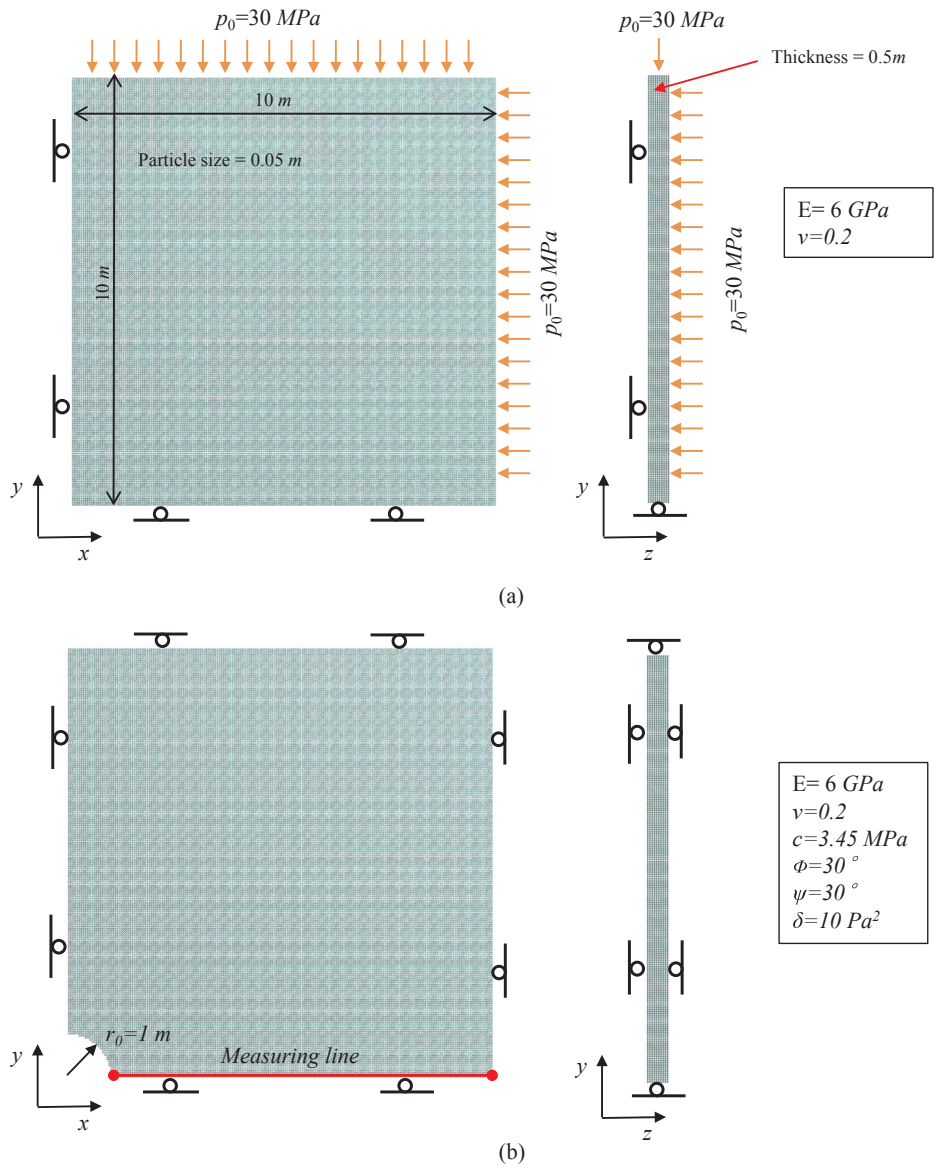

Fig. 8. Computational models of the tunnel excavation problem in an infinite plastic domain problem: (a) model and boundary conditions for the initial stress calculation; (b) model and boundary conditions for the tunnel excavation calculation.

measuring point and the boundary conditions is originating from the inhomogeneous deformation within the cube. This mismatch can be reduced by increasing the number of particles. To further address this mismatch, in the following, a more complex boundary value problem with the same material parameters will be conducted.

3.2. A plastic plate with circular hole under compression

In this section, the same material parameters and lattice configuration as the previous example are adopted for a more complex boundary value problem. The computational model of a plate with circular hole is shown in Fig. 6a. The bottom surface is fixed in all directions while a displacement of 2 mm is gradually applied to the top surface. This amount of loading is selected to be large enough to cause the specimen to yield. The dimensions of the model are 50 mm × 100 mm × 10 mm. The model is made up of 46,840 particles with a diameter of 1 mm. A measuring line 1–1 is inputted into the computational model to extract the displacements along the x and y directions. As a comparison, the Finite Volume Method (FVM) with the explicit scheme is adopted as the numerical reference solution; the code FLAC3D [16] was adopted in this work. The corresponding computational model of the FVM is shown in Fig. 6b. The same dimensions, material parameters, and boundary conditions were used in the DLSM and FVM. In this work, the OpenMP [12] is adopted to parallelize the plastic DLSM code. We have tested the computational time for this problem with a different number of threads (CPUs). With increasing the number of threads, the computational time of both the elastic DLSM and the plastic DLSM are all decreasing, i.e., the parallel implementation for the plastic DLSM is effective. The computational time of the plastic DLSM is found to not be increased much compared with its elastic counterpart. Therefore, the plastic implementation of the DLSM is well suited for parallel computing.

Fig. 7 shows the numerical results predicted by the plastic DLSM and FVM; a good agreement is found between them. The dilation angle has an apparent influence of the displacement in the x-direction, as is well captured by the plastic DLSM (see Fig. 7a). For the displacement in the y-direction, a small change is observed for both the plastic DLSM and FVM. The plastic DLSM is sensitive to capturing the small variation of plastic deformation in the x-direction. Although the elemental test (Section 3.1) with a small number of particles did not provide a good

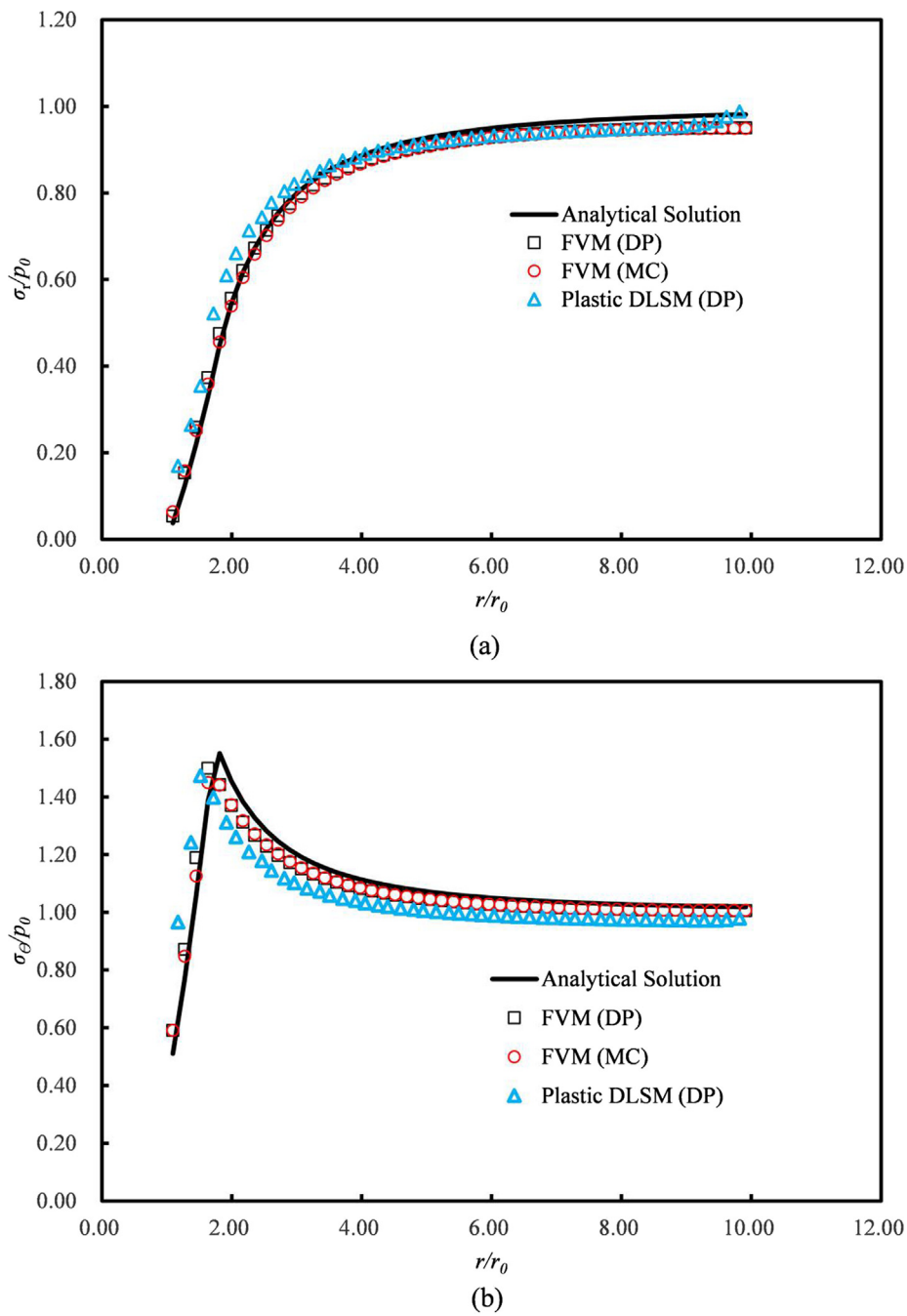

Fig. 9. Comparison between the analytical, the plastic DLSM and the FVM solutions: (a) the radius stress along the measuring line, and (b) the angular stress results along the measuring line.

fitting over the analytical solution, a computational model with a large number of particles can reproduce a good solution for a more complex boundary value problem. In this example, the FVM is used as the reference solution. In the following, a classical plastic boundary value problem will be further solved by the analytical solution, the FVM, and the plastic DLSM.

3.3. Cylinder tunnel excavation in an infinite medium

In this example, the plastic DLSM is further applied to solve a classical plastic boundary value problem in tunneling engineering. For the structure of underground spaces, the rock mass has an initial stress, namely, in-situ stress. When a tunnel is excavated, the stress around the tunnel will be redistributed, and the surrounding area may turn into a plastic state. Salençon [17] provided the analytical solution (plane strain condition) of a cylindrical tunnel excavated in rock masses based on the Mohr-Coulomb plastic model. Here, we give the corresponding solution when the internal pressure is zero. The radial and hoop stresses in the plastic zone are given as

$$\frac{\sigma_r}{p_0} = \frac{c}{p_0 \tan\phi\sqrt{1-\sin\phi}}\left[1-\left(\frac{r}{r_0}\right)^{\frac{2\sin\phi}{1-\sin\phi}}\right] \tag{47}$$

$$\frac{\sigma_\theta}{p_0} = \frac{c}{p_0 \tan\phi\sqrt{1-\sin\phi}}\left[1-\frac{1+\sin\phi}{1-\sin\phi}\left(\frac{r}{r_0}\right)^{\frac{2\sin\phi}{1-\sin\phi}}\right] \tag{48}$$

where r_0 is the tunneling radius, p_0 is the absolute value of the

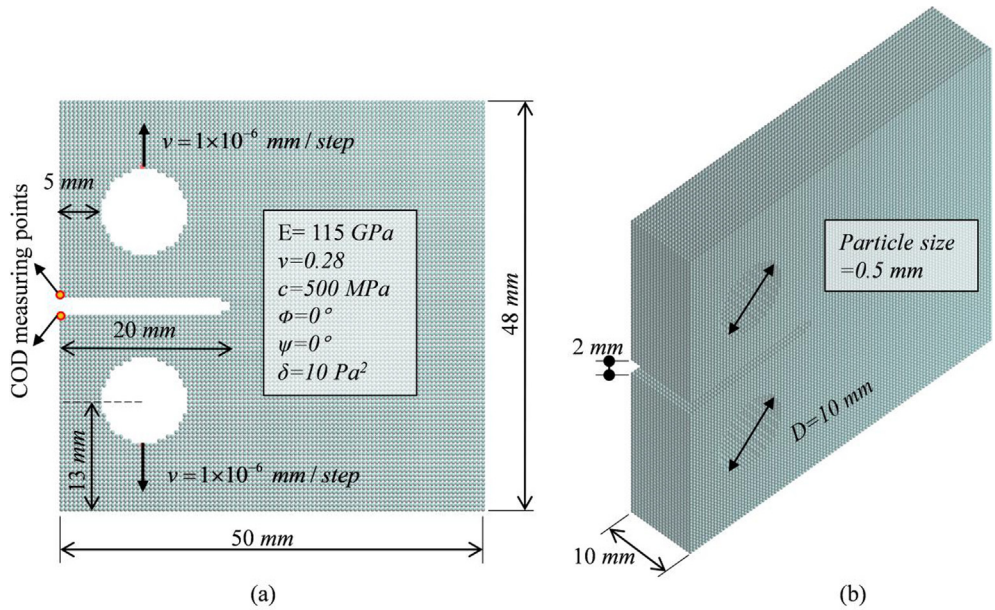

Fig. 10. Computational model of the plastic fracture of a titanium alloy plate problem: (a) 2D view, and (b) 3D view.

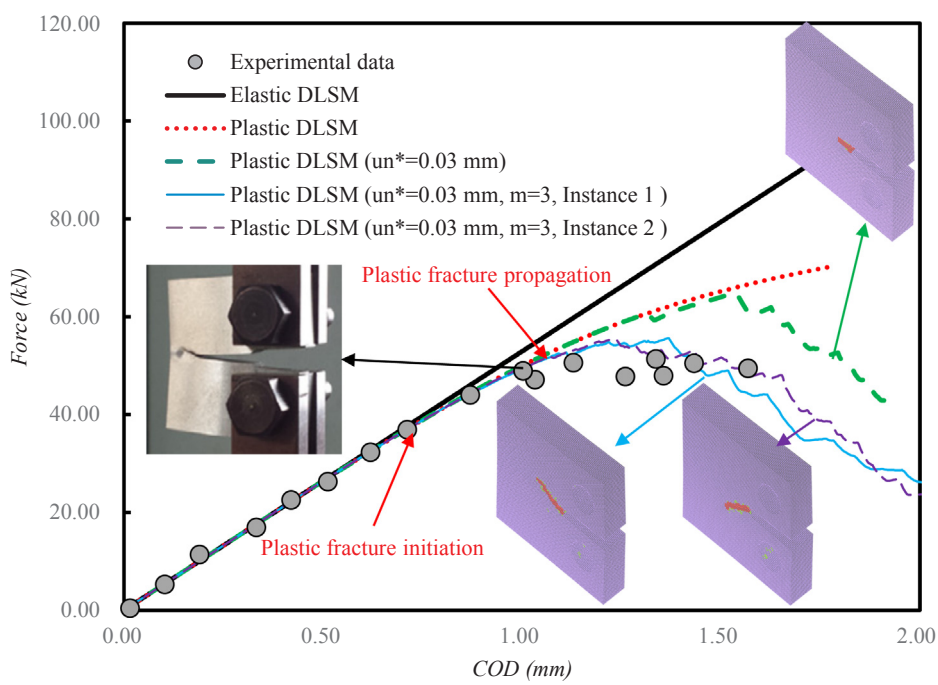

Fig. 11. Numerical prediction of the plastic DLSM and the corresponding experimental results from [5].

initial pressure (in situ stress), c is the cohesion, and ϕ is the friction angle. The stresses in the elastic zone are given as

$$\frac{\sigma_r}{p_0} = -1 + \left(2 - \sin\phi - \frac{c}{p_0}\cos\phi\right)\left(\frac{2cR_p}{r_0 r}\sqrt{\frac{1+\sin\phi}{1-\sin\phi}}\right)^2 \tag{49}$$

$$\frac{\sigma_\theta}{p_0} = -\frac{\sigma_r}{p_0} - 2 \tag{50}$$

where R_p is the radius of the plastic zone that can be further given as

$$\frac{R_p}{r_0} = \left[(1-\sin\phi)\left(1 + \frac{\sqrt{1-\sin\phi}\,\tan\phi p_0}{c}\right)\right]^{\frac{1-\sin\phi}{2\sin\phi}} \tag{51}$$

To simulate the excavation process, a two-stage calculation is used. As shown in Fig. 8a, the first stage is to obtain the initial stress by solving a static problem. The boundary conditions are shown in Fig. 8a in the case that a uniform pressure is applied to the surfaces of the model. After the calculation, particle displacements are inputted for the calculation of the 2nd stage, as shown in Fig. 8b, in which all the surfaces are fixed in their normal direction. The model size is taken as ten times of the tunnel's radius (1 m), e.g., 10 m in this example, which is a typical setting for underground tunneling analysis. The material parameters are selected as $E = 6$ GPa, $\nu = 0.2$, $c = 3.54$ MPa, $\phi = 30^\circ$, and $\psi = 30^\circ$ (associative flow rule). As a comparison, the FVMs with both the DP and MC plastic models were also solved. For FLAC3D (the FVM code [16]), the in-situ stress is inputted as an initial stress condition rather than using a two-stage simulation.

Fig. 9 shows the corresponding results of the analytical solution, the

DLSM, and the FVM. The numerical prediction by the plastic DLSM with the smoothed DP agrees well with the corresponding analytical solution and numerical results of the FVM with the DP and MC models. The divergent results obtained from the two-stage calculation adopted in this work cause a slight deformation at the 2nd stage computational model. From this example, we can further confirm that the plastic DLSM is able to solve plastic boundary value problems.

3.4. Plastic fracturing of a titanium alloy plate

As we have declared, the reason for selecting the DP to the DLSM is its simplicity and universality. When the friction angle ϕ is zero, the selected model can automatically turn into the Von-Mises model for metal. In the following, the plastic DLSM will be further applied to modeling plastic fracturing of metal. In this example, the plastic fracture test of a titanium alloy plate conducted by Ding et al. [5] will be further modeled by the plastic DLSM. A full 3D model is adopted; the corresponding specimen geometry and loading condition are shown in Fig. 10. The corresponding material parameters are directly taken from [5]. The elastic modulus is 115 GPa, Poisson's ratio is 0.28, and the cohesion is 500 MPa. Two measurement points (see Fig. 10a) were inserted to record the corresponding Crack Opening Displacement (COD) during the simulation. The reaction force at the velocity loading boundary was also recorded. The COD versus reaction force curve recorded in the experimental test [5] was used for verification.

First, we conducted numerical simulation using the elastic DLSM. As shown in Fig. 11, the elastic results provided a nice fit over the initial range. From this result, we can conclude that the boundary conditions and elastic parameters are reasonable. Nevertheless, the elastic modeling results will deviate from the experimental curve at a certain range (see Fig. 11). When the plasticity DLSM is used, the results will fit the corresponding plastic range curve, whereas it will also deviate for a later stage because a plastic model cannot reproduce the experimental results involving fracturing. Thus, the simple bond failure criterion is adopted with a failure parameter $u_n^* = 0.03$ mm. As shown in Fig. 11, the numerically predicted curve will turn downward relative to the experimental one. However, a good match is still not achieved. When we introduce the heterogeneity of the breakage of bonds through a Weibull distribution function as given in Eqs. (35) and (36), a better fitting can be achieved when $m = 3$. We consider that the plastic fracture initiation and propagation points can be marked as the deviation points as shown in Fig. 11.

The experimental data were also generated from two physical tests [8], and the variation of the final stage should originate from the failure heterogeneity of the material. The failure patterns of these numerical models considering fracturing are shown in Fig. 11. The fracture surface is straight for the homogeneous model, whereas it loses symmetry for these heterogeneous models. This phenomenon was also observed experimentally (see Fig. 11). However, the loss of symmetry in the experimental test can be induced by many factors, e.g., the material defects, the altering physical boundary conditions for unknown reasons, etc. Therefore, including a random distribution in the bond failure parameter appears to be a reasonable solution.

4. Conclusions

Because of the inconsistency between the constitutive model of the LSM and the plastic constitutive model of continuum mechanics, the implementation of plasticity to the LSM is difficult. In this work, a framework is developed for the DLSM to directly implement plasticity. The particle strain and plastic strain are used as the interface between the DLSM and the plastic constitutive model. Using this framework, a smoothed DP model is successfully implemented to the DLSM. The applicability and correctness of the plastic DLSM are verified from a number of numerical examples. It is concluded that the plastic DLSM is stable and enables solution of plastic boundary value problems under various conditions, including fracturing. The developed framework integrates the advantage of DLSM on modeling fracturing problem and the ability of the classical plastic model on describing the plastic deformation of materials, which may also be applicable to other discrete numerical models. Nevertheless, the proposed framework is still limited to small deformation assumption. How to include large deformation, more complex plastic models and dynamic constitutive models of jointed rock masses [18,19] will be our future work.

Acknowledgements

This research is financially supported by the National Natural Science Foundation of China (Grant No. 1177020290) and the State Key Laboratory for Geomechanics and Deep Underground Engineering, CUMT (Grant No. SKLGDUEK1706).

References

[1] Wong KW. Three-dimensional multi-scale hydraulic fracturing simulation in heterogeneous material using Dual Lattice Model PhD thesis University of Cambridge; 2018.
[2] Zhao G-F. Developing a four-dimensional lattice spring model for mechanical responses of solids. Comput. Meth. Appl. Mech. Eng. 2017;315:881–95.
[3] Reck M. Lattice spring methods for arbitrary meshes in two and three dimensions. Int. J. Numeri. Meth. Eng. 2017;110(4):333–49.
[4] Laubie H, Radjaï F, Pellenq R, Ulm FJ. A potential-of-mean-force approach for fracture mechanics of heterogeneous materials using the lattice element method. J. Mech. Phys. Solids 2017;105:116–30.
[5] Ding J, Zhang Z, Yang F, Zhao Y, Ge X. Plastic fracture simulation by using discretized virtual internal bond. Eng. Fract. Mech. 2017;178:169–83.
[6] Jiang C, Zhao G-F. Implementation of a coupled plastic damage distinct lattice spring model for dynamic crack propagation in geomaterials. Int. J. Numeri. Analy. Meth. Geomech. 2018;42(4):674–93.
[7] Chen H, Lin E, Liu Y. A novel Volume-compensated particle method for 2D elasticity and plasticity analysis. Int. J. Solids Struct. 2014;51:1819–33.
[8] Zhao G-F, Fang J, Zhao J. A 3d distinct lattice spring model for elasticity and dynamic failure. Int. J. Numeri. Analy. Meth. Geomech. 2011;35(8):859–85.
[9] Buxton GA, Care CM, Cleaver DJ. A lattice spring model of heterogeneous materials with plasticity. Model. Simul. Materi. Sci. Eng. 2001;9(6):485–97.
[10] Cheng M, Liu W, Liu K. New discrete element models for elastoplastic problems. Acta Mech. Sin. 2009;25(5):629–37.
[11] Guozden TM, Jagla EA. Fatigue crack propagation in a quasi-one-dimensional elasto-plastic model. Int. J. Solids Struct. 2012;49(23–24):3224–32.
[12] Zhao G-F, Fang J, Sun L, Zhao J. Parallelization of the distinct lattice spring model. Int. J. Numer. Analy. Meth. Geomech. 2013;37(1):51–74.
[13] Jiang C, Zhao G-F, Khalili N. On crack propagation in brittle material using the distinct lattice spring model. Int. J. Solids Struct. 2017;118–119:1339–51.
[14] Tang CA, Liu HY, Zhu WC, Yang TH, Li WH, Song L, et al. Numerical approach to particle breakage under different loading conditions. Powder Tech. 2004;143–4:130–43.
[15] Ma GW, Wang XJ, Ren F. Numerical simulation of compressive failure of heterogeneous rock-like materials using sph method. Int. J. Rock Mech. Min. Sci. 2011;48(3):353–63.
[16] Itasca Consulting Group, Inc. FLAC3D –Fast Lagrangian Analysis of Continua in 3 Dimensions, Minneapolis, Itasca, 2012.
[17] Salençon J. Contraction quasi-statique d'une cavite a symetrie spherique ou cylindrique dans un milieu elastoplastique. Ann. Ponts Chaussees 1969;4:231–6.
[18] Zhao J. Applicability of Mohr-Coulomb and Hoek-Brown strength criteria to the dynamic strength of brittle rock. Int. J. Rock Mech. Min. Sci. 2000;37(7):1115–21.
[19] Liu Y, Li H, Zhao J, Li J, Zhou Q. UDEC simulation for dynamic response of a rock slope subject to explosions. Int. J. Rock Mech. Min. Sci. 2004;49(7):599–604.